

Eliminating Skyrmiion Hall Effect in Ferromagnetic Skyrmions

Xudan Zhang, Guolin Wan, Jie Zhang, Yan-Fang Zhang, Jinbo Pan,* and Shixuan Du*



Cite This: <https://doi.org/10.1021/acs.nanolett.4c02060>



Read Online

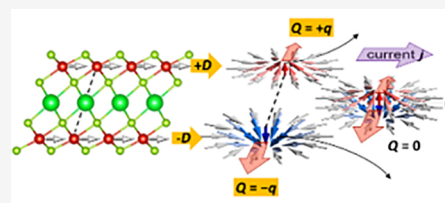
ACCESS |

Metrics & More

Article Recommendations

Supporting Information

ABSTRACT: Skyrmiion Hall effect (SkHE) remains an obstacle for the application of magnetic skyrmions. While methods have been established to cancel or compensate SkHE in artificial antiferromagnets and ferrimagnets, eliminating intrinsic SkHE in ferromagnets is still a big challenge. Here, we propose a strategy to eliminate SkHE by intercalating nonmagnetic elements into van der Waals bilayer ferromagnets featuring in-plane ferromagnetism. The in-plane magnetism, along with a delicate balance among exchange interactions, Dzyaloshinskii–Moriya interactions (DMI), and magnetocrystalline anisotropy, creates interlayer bimerons/quadmerons, whose polarity can be controlled by DMI. Opposite DMI in the upper and lower layers results in opposite polarity and topological charge number Q -locking of topological spin texture, therefore, eliminating the SkHE. By intercalating Sr (Ba) in bilayer VSe₂, we identify ten topological magnetic structures with zero topological charge number. Furthermore, we present a phase diagram illustrating diverse magnetic configurations achievable within the bimagnetic atomic layer, offering valuable guidance for future investigations.



KEYWORDS: ferromagnetic skyrmions, topological charge number, Dzyaloshinskii–Moriya interaction, skyrmiion Hall effect, intercalated two-dimensional structure

Magnetic skyrmions, characterized by a particle-like magnetic whirl with nontrivial topology,^{1–5} have been intensively studied^{2,4–10} due to their intriguing fundamental physics, and promising applications in advanced spintronics, e.g., the state-of-the-art racetrack memory.^{8–10} A key aspect of their role in racetrack memory involves the efficient control of creation, motion, and detection of skyrmions. Numerous approaches have been proposed to generate diverse types of skyrmions, including Bloch skyrmion,^{11,12} Néel skyrmion,^{11,13} meron,^{3,14–17} bimeron,^{18–21} antiskyrmion,^{22,23} and so on.^{24,25} Despite notable progress, the practical implementation of skyrmions in spintronic devices remains elusive due to many challenges, such as its lateral motion driven by Magnus force,^{26–28} which is known as the skyrmiion Hall effect (SkHE).^{29,30}

The Magnus force is proportional to the topological charge number Q and its direction is determined by sign of Q .^{14,31,32}

Q is defined as $Q = \frac{1}{4\pi} \int \mathbf{m}(\mathbf{r}) \cdot \left[\frac{\partial \mathbf{m}(\mathbf{r})}{\partial x} \times \frac{\partial \mathbf{m}(\mathbf{r})}{\partial y} \right] d^2 r$ ($\mathbf{m}(\mathbf{r})$ is the magnetization density), which can be obtained by counting the number of times that magnetization vector field m wraps the Bloch sphere.³³ From this perspective, skyrmions emerging in ferromagnetic materials, such as Bloch skyrmion, Néel skyrmion, meron, and bimeron with integer or half-integer Q , would laterally drift to the edge and consequently be destroyed. Until now, strategies to eliminate the SkHE on artificial antiferromagnetic system and ferrimagnetic systems are well-known,^{17,27,28,34,35} while eliminating SkHE in ferromagnetic systems is still a big challenge. Recently, two strategies in experiments to eliminate SkHE in ferromagnetic

systems were reported, including electric field manipulation³⁶ and helical stripe domain modulation.³⁷ The generation of intrinsic SkHE-free ferromagnetic skyrmion, however, remains unclear.

In this paper, based on a double-magnetic-atomic-layer interaction model, we propose a novel mechanism to eliminate the SkHE in in-plane ferromagnetic systems characterized by a reversal Dzyaloshinskii–Moriya interaction (DMI) within the neighboring two ferromagnetic layers. The in-plane ferromagnetism accompanying with appropriate D/\sqrt{JK} (J is the intralayer magnetic exchange coupling, K is the magnetocrystalline anisotropy) give birth to meron or bimeron, while the interlayer symmetry (S) insures the reversal D (rD) within the two magnetic layers, thus generating opposite Q within the two magnetic layers, resulting in a zero Q (Q) of the locked interlayer bimeron (or interlayer quadmeron) and the absence of SkHE. We name such a mechanism $SrDQ$. The $SrDQ$ mechanism is verified by two intercalated structures MV_2Se_4 ($M = Sr, Ba$), and 10 new topological magnetic structures (5 types) with zero Q are obtained. In addition, the evolution of topological spin textures and Q under an external magnetic field and the variation of magnetic interaction parameters are

Received: April 30, 2024

Revised: August 8, 2024

Accepted: August 13, 2024



mapped out. Micromagnetic simulations verify the elimination of SkHE under a current density lower than $5500 \times 10^{10} \text{ A/m}^2$.

The topological magnetic structure can be solely determined by three distinct numbers (m, p, γ), where m, p , and γ are vorticity, polarity, and helicity, respectively.^{3,29,32} The magnetic density of a topological spin texture can be expressed as

$$\mathbf{m}(\mathbf{r}) = \left(\left(\frac{x}{r} \cos \gamma - m \frac{y}{r} \sin \gamma \right) \sin \left(\frac{\pi}{r_0} r \right), \right. \\ \left. \left(\frac{x}{r} \sin \gamma + m \frac{y}{r} \cos \gamma \right) \sin \left(\frac{\pi}{r_0} r \right), p \cos \left(\frac{\pi}{r_0} r \right) \right)$$

where r_0 is the radius.³² The topological charge number Q is jointly determined by vorticity m and polarity p , and can be expressed by $Q = m \cdot p$ (see details in SI section 1.1), where $p = -\frac{1}{2} \cos \theta(r)|_{r=0}^\infty = 0$ and $m = \frac{1}{2\pi} \Phi(\phi)|_{\phi=0}^{2\pi} = 0$. The Magnus force F is proportional to Q , $F = G\hat{z} \times j$, where $G = 4\pi Q$, the zero net Q results in canceled F . Therefore, the topological spin texture moves without transverse motion, that is, the canceled SkHE. Despite the discovery of magnetic skyrmions in various 2D ferromagnetic monolayers, they typically exhibit nonzero Q , we then turn to the double-magnetic-atomic-layer systems. The opposite Q occurring in top and bottom magnetic layers indicates that one of their polarities and vorticities is the same, while the other is opposite. For the interlayer Bloch and Néel type bimerons under interlayer ferromagnetic coupling, their polarity and vorticity in each layer are fixed by the same outermost spin orientation, resulting in the same Q in both layers (as shown in Figure S3); thus, they cannot harbor FM-coupled interlayer biskyrmion with zero Q . However, for Merons and bimerons, their polarity cannot be fixed by the outermost spin orientation, thereby offering a potential platform to achieve zero Q .

Figure 1 depicts two strategies to design interlayer bimeron with zero Q , which is vertically stacked by two merons. The noncollinear spin textures of a material is often attributed by DMI,^{38,39} the Hamiltonian form of DMI is given by $H = -\sum_{i,j} \mathbf{D}_{ij} \cdot (\mathbf{S}_i \times \mathbf{S}_j)$. In magnetic monolayers and bulk materials, the broken central inversion is a necessary condition for the appearance of D , which arises from spin-orbit coupling.⁴⁰ In a double-magnetic atomic-layer system with central inversion (case 1), there may be a net D hidden within each layer, which can be explained by symmetry operation. Given a symmetry operator $\hat{A} = \{Alt\} \in$ space group G performing on the DM vector D , where A is the rotational part, $A \in SO(3)$ and t is the translational part, D turns into D' , there is the transformation formula: $D' = \det[A]AD$, as derived from SI section 2.2. We obtain

$$\mathbf{D}_{k'j'} = -\mathbf{D}_{j'k'} = -\mathbf{D}_{jk} = (-D_x, -D_y, -D_z)^T \quad (1)$$

i.e., the top and bottom magnetic layers have opposite DMI values. Such a result is easy to understand since the system with inversion symmetry does not contain net DMI. However, symmetry breaking exists in each magnetic layer, leading to the generation of DMI in each layer. Therefore, the DMI values in the upper and lower layers has opposite signs, while for the mirror symmetry (case 2, see details in SI section 2.3)

$$\mathbf{D}_{j'k'} = (-D_x, -D_y, D_z)^T \quad (2)$$

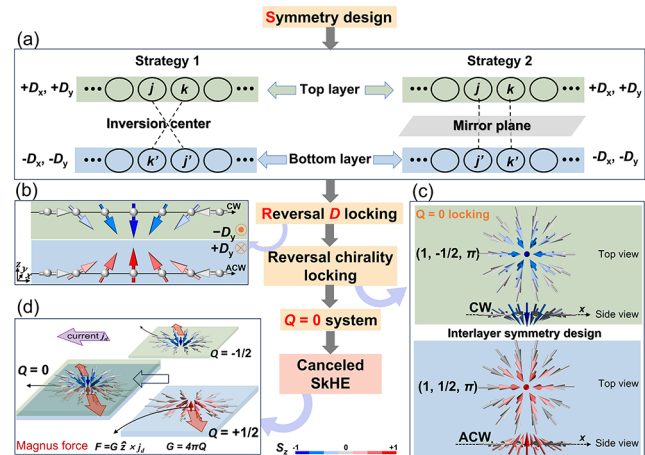


Figure 1. Design strategy of SrDQ to eliminate SkHE in double-magnetic-atomic-layer ferromagnets. (a) Schematics of designed systems containing two ferromagnetic layers connected by inversion symmetry or mirror symmetry. The j and k atoms in the top layer correspond to the j' and k' atoms in the bottom layer due to the inversion or mirror symmetry. The ferromagnetic upper and lower layers have reversal DM coefficients (D_x, D_y) and $(-D_x, -D_y)$, respectively. (b) Schematic shows the relationship between the sign of D_y and the chirality along the x direction. Reversal of D results in reversal of chirality. ACW and CW represent the anticlockwise and clockwise chirality, respectively. (c) Example of $Q = 0$ locked interlayer Néel bimerons. In case of the same m and opposite chirality, the opposite polarities in the ferromagnetic double layers are more energy favorable, resulting in the opposite Q within the two layers and zero of the whole system. (d) Schematics of the canceled skyrmion Hall effect of the SrDQ system. Q determines direction of Magnus force (labeled by pink arrows). Driven by the horizontal current j_d (labeled by purple arrow), a single meron drifts to the boundary and finally disappears (labeled by black arrow). However, the zero Q in the interlayer bimeron leads to a complete cancellation of the Magnus forces, resulting in the movement of skyrmion along the current without transverse motion.

It has similar explanations as following. The mirror symmetry connected homostructure does not contain net in-plane DMI; however, in-plane DMI exists in each magnetic layer. Therefore, the in-plane DMI in the upper and lower layers have opposite signs.

The in-plane D dominates the chirality of the 2D topological magnetic materials. A reversal D locking of bilayer magnetic layers leads to the same vorticity and opposite chirality^{41–44} locking, as shown in Figure 1b. The topological magnetic structures with opposite chirality and the same vorticity (m) locking in the upper and lower layers, when mapped onto the two degrees of freedom of the topological magnetic structure, can be divided into two scenarios: Case 1, $p_{top} = -p_{bottom}, \gamma_{top} = \gamma_{bottom}$, resulting in zero Q of the interlayer bimeron; Case 2, $p_{top} = p_{bottom}, \gamma_{top} = -\gamma_{bottom}$ or $\gamma_{top} = \pi - \gamma_{bottom}$ resulting in a reduplicated Q . Taking Néel-type merons as an example, as shown in Figure 1c, if the top layer's Néel meron is characterized as $(1, -1/2, \pi)$, due to the reversal D locking, the possible merons occurring in the bottom layers are locked as $(1, 1/2, \pi)$ and $(1, -1/2, 0)$; see details in Figure S4.

The Hamiltonian for nearest neighbor interlayer interaction of the systems can be expressed as

$$H_{bt} = \sum_{i',i} \mathbf{s}_{bi}' \cdot \mathbf{j}_{bt} \cdot \mathbf{s}_{ti} \quad (3)$$

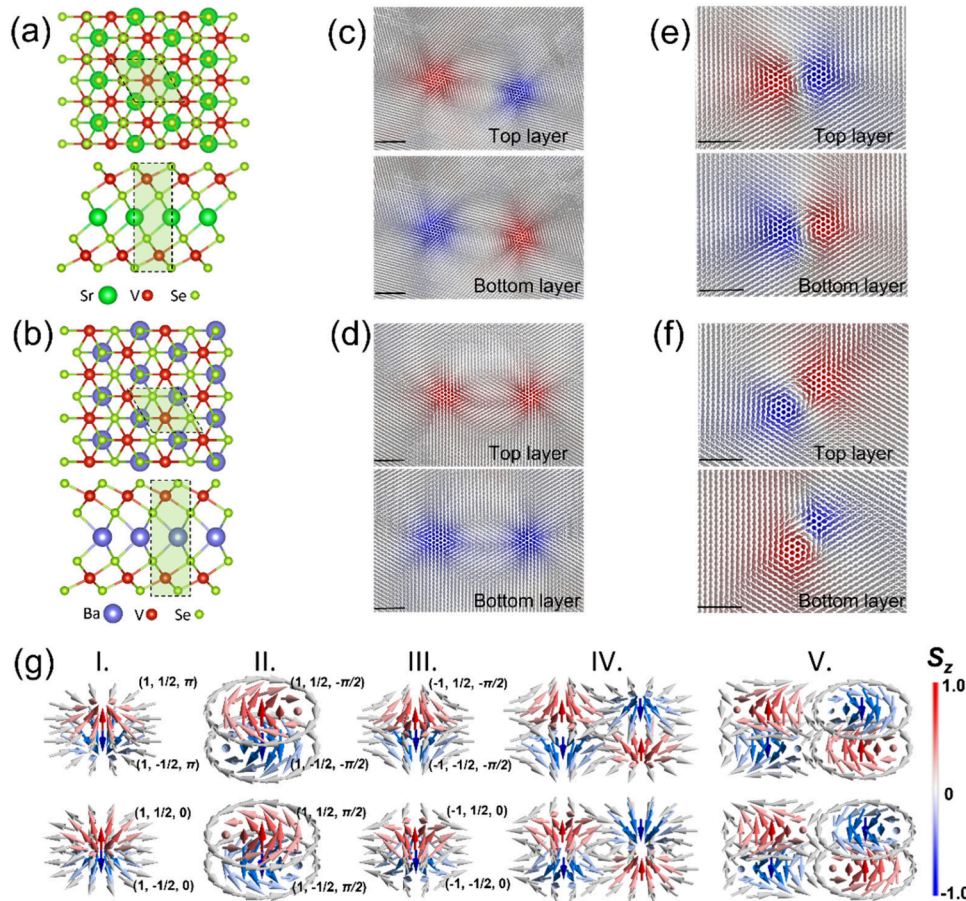


Figure 2. Structures and topological spin textures of MV_2Se_4 monolayers ($M = Sr, Ba$). (a) and (b) Top and side views of SrV_2Se_4 and BaV_2Se_4 , respectively. The light green area indicates a unit cell. (c)–(f) Monte Carlo simulations of magnetic configurations of MV_2Se_4 without external field. (c) and (e) The zoom-in spin textures of SrV_2Se_4 on interlayer bimeron and interlayer quadmeron, respectively. (d) and (f) The zoom-in spin textures of BaV_2Se_4 on interlayer bimeron and interlayer quadmeron, respectively. The gray spins represent in-plane ferromagnetic backgrounds, while colors are assigned for the positive (red) or negative (blue) out-of-plane components of spins. (g) Five types of spin texture forms with $SrDQ$ in MV_2Se_4 , as can be distinguished by (m, p, γ) . The black line segment inserted in all panels indicates a scale bar of 5 nm.

where ti represents the top atom at i site, and bi' represents the bottom atom at i' site, and J_{bt} is the interlayer coupling between the upper and lower layers. Assuming that m radial lines emit from the core center of meron, according to the derivation in [SI section 3.1](#), the energy of interlayer coupling of topological structures can be expressed as

$$E_{bt} = \begin{cases} (m-1) \cdot J_{bt} \cdot S^2, & \text{case 1: } Q = 0 \\ -(m-1) \cdot J_{bt} \cdot S^2, & \text{case 2: } Q = -1 \end{cases}$$

$$m > 1, m \in N \quad (4)$$

The ferromagnetic coupling between the upper and lower layers prefers opposite p locking. Finally, the $(1, -1/2, \pi)$ meron of the top layer is locked with the $(1, 1/2, \pi)$ meron of the bottom layer, as shown in [Figure 1\(c\)](#), thus $Q = 0$, while antiferromagnetic coupling favors the same p locking, thus $Q = -1$ (see [Figure S6](#)). The above mechanism is universal to all topological magnetic structures whose polarity is not fixed by the ferromagnetic background, such as interlayer quadmeron. The zero Q case, results in the elimination of SkHE, as illustrated in [Figure 1d](#).

In order to identify promising candidates, we focus on materials with in-plane magnetism and substantial interlayer interaction. The in-plane ferromagnetism is conducive to

hosting half-integer- Q skyrmions,[45,46](#) while substantial interlayer interaction serves to stabilize interlayer bimeron (and interlayer quadmeron). The intercalated structures[47–49](#) consist of bilayer magnetic materials and an intercalated atomic layer have potential to fulfill these two requirements. We take the experimental realized two-dimensional (2D) magnetic material $1T\text{-}VSe_2$ [50–53](#) as an example to identify potential candidates, some atom intercalated structures have been synthesized recently.[54](#) High throughput calculations are performed to screen ideal intercalated element sandwiched with two VSe_2 layers and find that the intercalated alkaline earth metals Sr or Ba would result in an intrinsic in-plane ferromagnetism and a substantial interlayer coupling. Eight stacking modes are considered to identify the ground state structure ([SI sections 4.1 and 4.2](#)). The ground state structures of SrV_2Se_4 and BaV_2Se_4 are shown in [Figure 2a,b](#), which have central-inversional and mirror symmetry, respectively. These structures are thermodynamically, dynamically, and thermally stable as shown in [Table S3](#), [Figures S9 and S10](#). Both structures have C_{3v} symmetry, and in-plane ferromagnetism with magnetic moment of $2 \mu_B$ per V atom ([Figures S11–S13 and S14](#)). According to Moriya rules, C_3 symmetry ensures that the average contribution of the out-of-plane D component is zero for each layer, while the in-plane component remains nonzero. The in-plane DMI of MV_2Se_4 ($M = Mg, Ca, Sr, Ba$)

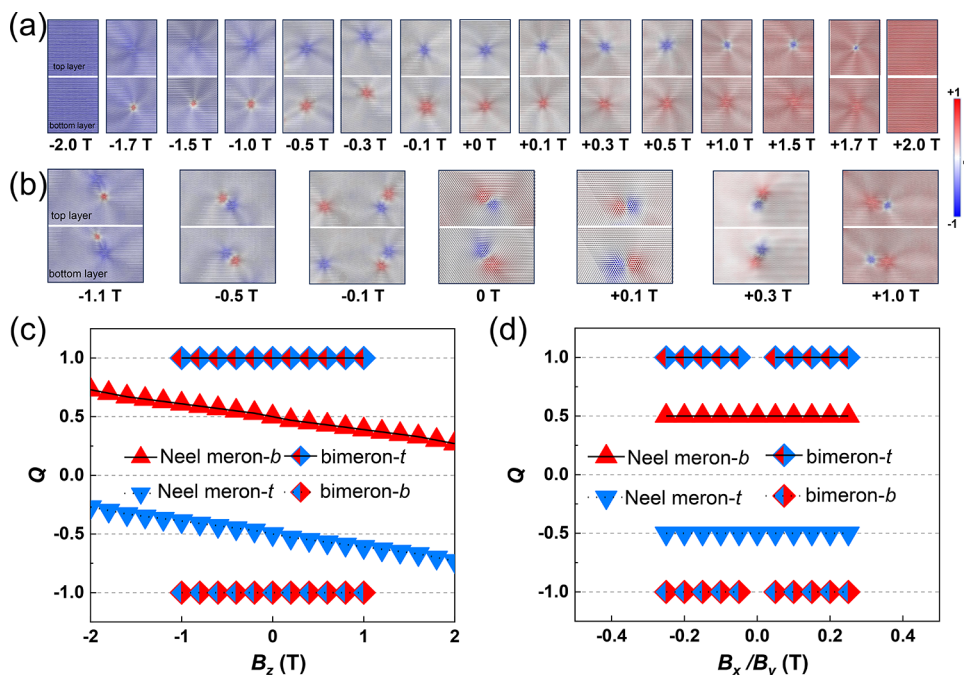


Figure 3. Evolution of SrDQ systems under external magnetic field. (a) and (b) The evolution of type III and V topological magnetic structures under magnetic field along the z direction, respectively. (c) and (d) The evolution of topological charge number Q values under external magnetic field along the z and x/y directions, respectively.

in one magnetic layer is shown in Figure S15(a). Mg and Ca exhibit a much weaker SOC effect than Sr and Ba, resulting in much smaller in-plane DMI of MgV_2Se_4 and CaV_2Se_4 compared to those of SrV_2Se_4 and BaV_2Se_4 , and cannot generate interlayer bimeron. In Sr and Ba intercalated structures, Sr and Ba primary contributions to ΔE_{SOC} in SrV_2Se_4 and BaV_2Se_4 (Figure S15(b)). The relatively heavy nonmagnetic Sr/Ba atoms act as effective sites for spin-orbit coupling scattering, which is an indication of Fert-Levy mechanism and crucial for DMI generation.

The generalized quadratic Heisenberg spin Hamiltonian model⁵⁵ and the four-state method^{56,57} are employed to calculate the magnetic coupling parameters for both intra- and interlayer interactions, listed in Tables S4 and S5. Monte Carlo (MC) simulations are then performed to determine low-energy spin textures, as shown in Figure 2c–f. Due to the reversal of D locking, m and γ of the meron or bimeron at top and bottom layers are the same, while Q and p are opposite. Distinguished by m , p , and γ , 10 topological magnetic structures with SrDQ are obtained (as illustrated in Figure 2g); according to its different in-plane magnetization, i.e., m and γ , they can be divided into five groups: interlayer Néel bimeron (type I), interlayer Bloch bimeron (type II), interlayer anti bimeron (type III), interlayer anti-Neel quadmeron (type IV), and interlayer anti-Bloch quadmeron (type V), respectively. Without an external field, the sizes of Types I–III are about 4.8 nm, while those of Types IV and V are about 4.8×7.2 nm². The cores of two merons in each intralayer bimeron are separated by a distance of around $8a$ (a is the lateral lattice constant), aligning with the lowest energetic configuration for a bimeron reported in ref 58. From Figure S17 we can see that the topological magnetic structure of SrV_2Se_4 is robust under 15 K. Since the transition temperature is mainly determined by the magnitude of the exchange interaction strength (Figure S18), increasing the exchange interaction strength will increase

the stability of the topological magnetic structure. As reported in previous literature,¹⁷ Tl_2NO_2 with AA' stacking possesses an exchange interaction value up to 30 meV, higher than that of SrV_2Se_4 (7 meV). Our MC simulation indicates that the interlayer bimeron/quadmeron generated in Tl_2NO_2 with AA' stacking can be stable up to 160 K.

Figure 3 illustrates the evolution of topological spin textures of the interlayer bimeron and interlayer quadmeron under a magnetic field. The topological spin textures remain undestroyed under external magnetic field 2.0 T. As shown in Figure 3a, if the sign of polarity and magnetic field B_z is the same, a single meron expands and would finally disappears with increasing of B_z . While the sign of polarity and magnetic field is the opposite, a single Meron contracts and would also finally disappear with an increase of B_z . Due to the opposite polarity in our studied interlayer bimeron, one meron expands, while the other contracts under nonzero B_z . In an interlayer quadmeron, the variation of each single meron under a magnetic field is similar, as illustrated in Figure 3b. The Q of the interlayer bimeron evolves with B_z is shown in Figure 3c. As can be seen, the absolute Q increases from 0.5 to around 0.7 as the single meron expands, while it decreases from 0.5 to 0.3 as the single meron contracts, resulting in a nonzero overall Q under the external field B_z smaller than 2.0 T. For interlayer quadmeron under the external field B_z , the Q remains zero. Such phenomena can be explained as following. The mapping of a two-dimensional meron to a three-dimensional space corresponds to a hemisphere. When B_z is applied on a meron, all spins of a meron add a polar angle θ' , by adding the angle integral over the corresponding hemisphere, Q is changed by a value of $\sin \theta'$, resulting in the continuously changed Q for interlayer bimeron. One bimeron consists of two merons with opposite polarity and vorticity. A broad expression for one bimeron of interlayer quadmeron (type IV and V) is $(1, \pm \frac{1}{2}, \gamma) / (-1, \mp \frac{1}{2}, \gamma')$, the other can be expressed as

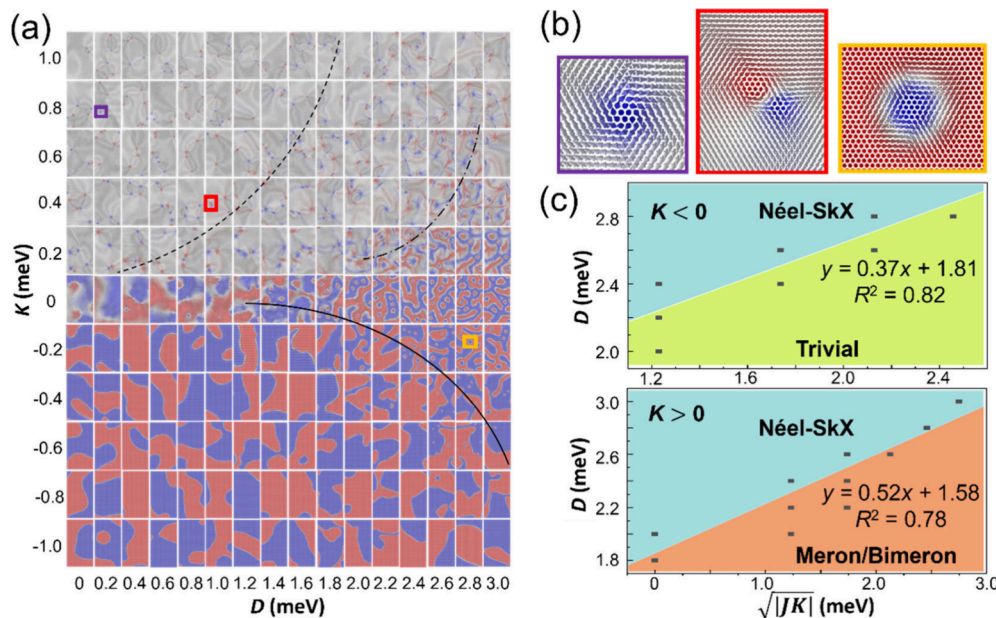


Figure 4. Phase diagram of the ferromagnetic bilayer with different reversal D and magnetocrystalline anisotropy K , where the intralayer exchange coupling parameter $J = 7.5$ meV. (a) The phase diagram of spin textures with different D and K , where the intralayer exchange coupling parameter $J = 7.5$ meV. (b) The zoom-in spin textures labeled by color boxes in (a). (c) Linear scaling relation between D and \sqrt{JK} of Néel-SkX/Meron and Néel-SkX/trivial boundary.

$(1, \mp\frac{1}{2}, \gamma)/(-1, \pm\frac{1}{2}, \gamma')$. The applied magnetic field along z direction result in an additional inclination θ' near the z axis to the overall topological spin texture. The core spin does not change its direction along the z axis, the vorticity m does not vary with the applied magnetic field, from eq S2.1.2,

$$\begin{aligned} p \rightarrow p' &= -\frac{1}{2}[\cos \theta]_{r=0}^{\infty} = \frac{1}{2}[\cos \theta]_{\pi/2-\theta'}^{0 \text{ or } \pi} \\ &= \pm\frac{1}{2} - \sin \theta' \end{aligned}$$

let $\alpha = \sin \theta'$, $\alpha < \frac{1}{2}$, there is

$$\begin{aligned} \left(1, \pm\frac{1}{2}, \gamma\right) &\xrightarrow{B_z} \left(1, \pm\frac{1}{2} - \alpha, \gamma\right), \\ \left(-1, \mp\frac{1}{2}, \gamma'\right) &\xrightarrow{B_z} \left(-1, \mp\frac{1}{2} - \alpha, \gamma'\right), \\ Q_{(1,\pm 1/2-\alpha,\gamma)} &= \left(\pm\frac{1}{2} - \alpha\right) \cdot 1, \\ Q_{(-1,\mp 1/2-\alpha,\gamma')} &= \left(\mp\frac{1}{2} - \alpha\right) \cdot (-1), \\ Q_{(1,\pm 1/2-\alpha,\gamma)} + Q_{(-1,\mp 1/2-\alpha,\gamma')} &= \\ \left(\pm\frac{1}{2} - \alpha\right) \cdot 1 + \left(\mp\frac{1}{2} - \alpha\right) \cdot (-1) &= \pm 1 \end{aligned} \quad (5)$$

under the external magnetic field B_z . The character of a bimeron $(1, \pm\frac{1}{2}, \gamma)/(-1, \mp\frac{1}{2}, \gamma')$ turns into a new form $(1, \pm\frac{1}{2} - \alpha, \gamma)/(-1, \mp\frac{1}{2} - \alpha, \gamma')$; hence, the Q value remains unchanged, as illustrated in Figure 3c. By extension, among multiple meron states, those with an integer Q are more stable than those with a half-integer Q under the external field B_z , the former Q keep unchanged. The Q values of interlayer

bimerons and quadmerons in MV_2Se_4 are both robust under the in-plane magnetic field smaller than 0.5 T. as shown in Figure 3d.

The impact of different magnetic interactions on the magnetic structure of double-ferromagnetic-atomic-layer systems is further investigated. We summarize in Figure 4a the phase diagram of spin textures as a function of D and K in the ferromagnetic bilayer systems with reversal D . $K > 0$ favors the in-plane ferromagnetism, while $K < 0$ favors the out-of-plane ferromagnetism. When $K > 0$, the meron state occurs at relatively small D values; as D increases, the meron phase moves toward a higher K , and bimeron/multiple-Meron states appear; With a further increase of D , the bimeron/multiple-Meron phase moves toward a higher K , and the domain walls and skyrmion states appear. The curve formed by the dash line is the dividing line between isolated meron state and bimeron/multiple-Meron state. The dashed and dotted curve is the dividing line between the bimeron/multiple meron state and the skyrmion state. When $K < 0$, the skyrmion state occurs at relatively small K values and large D values; as the magnitude of K increases, the skyrmion phase moves toward a higher D . The curve formed by the solid line is the dividing line between the skyrmion state and the trivial magnetic domain wall.

To facilitate the rational design of topological magnetic structures, a universal descriptor based on the magnetic parameters D , J and K can be established. We perform a linear fitting of the relationship between D and $\sqrt{|JK|}$, as demonstrated in Figure 4c, corresponding to the dashed and dotted curve and solid curve in Figure 4a. Prior studies on out-of-plane ferromagnetic monolayer systems with $K < 0$ indicated the emergence of the Néel-SkX phase require an appropriate $D/\sqrt{|JK|}$ slope ranging between 0.1 and 0.2.^{8,59,60} In the ferromagnetic bilayer system with out-of-plane ferromagnetism, the slope is 0.37. The interlayer ferromagnetic coupling in the Hamiltonian can be effectively considered as a finite built-in magnetic field. Consistent with previous

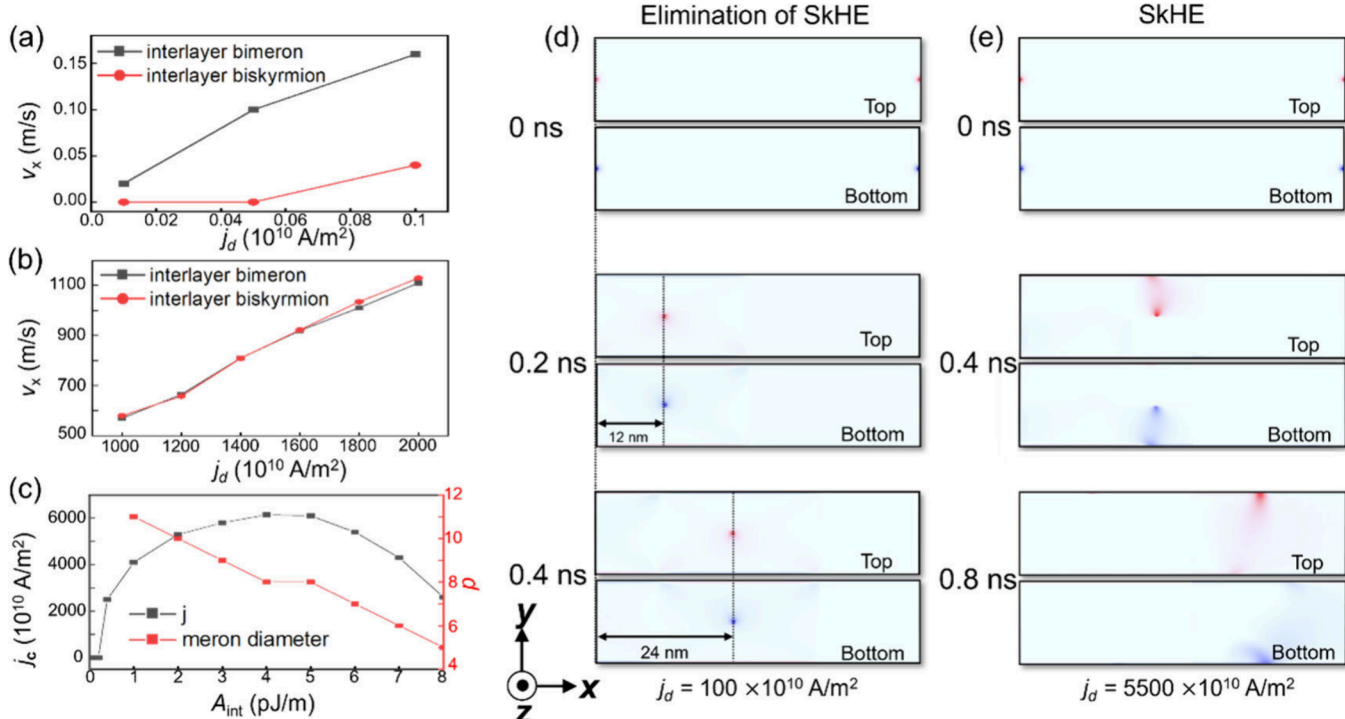


Figure 5. Current-driven motion of FM-coupled interlayer bimeron and AFM-coupled interlayer skyrmion. (a) and (b) The velocities of interlayer bimerons and interlayer skyrmions as functions of low and high driven current densities j_d , respectively. (c) The critical coupling current density j_c (black line) and the meron diameter d (unit: lattice constant) (red line) as a function of the interlayer FM exchange stiffness A_{int} . For the current density above the black curve, the interlayer bimerons will decouple. (d) and (e) Top views of the trajectories of an FM-coupled interlayer bimeron in the top and bottom FM layers at $j_d = 100 \times 10^{10} \text{ A/m}^2$ and $j_d = 5500 \times 10^{10} \text{ A/m}^2$, respectively. The size of the FM-coupled bilayer nanotrack is $512 \times 128 \text{ nm}^2$. $D = 3 \text{ mJ/m}^2$ and the interlayer exchange stiffness $|A_{\text{int}}| = 6 \text{ pJ/m}$, the Gilbert damping, and coefficient $\alpha = 0.3$ are used in the simulations.

research,⁵⁹ a stronger magnetic field correlates with a steeper slope, suggesting that multimagnetic-atomic-layer systems need a larger ratio of D and $\sqrt{|JK|}$ to stabilize the skyrmion phase. In the ferromagnetic bilayer system with in-plane ferromagnetism ($K > 0$), the criterion for the generation of Néel-SkX and meron/multimeron is derived as 0.52. $D/\sqrt{|JK|}$ slightly smaller than 0.52 is required to harbor meron.

Micromagnetic simulations are performed to investigate the dynamics and stability of interlayer bimerons at different driven current densities j_d . As shown in Figure 5a, FM-coupled interlayer bimeron exhibits a critical driven current density threshold of $\sim 0.01 \times 10^{10} \text{ A/m}^2$, an order of magnitude lower than that of the AFM-coupled interlayer skyrmion,²⁷ suggesting lower energy consumption. At current densities exceeding $1000 \times 10^{10} \text{ A/m}^2$, the velocities of FM interlayer bimerons reach the same magnitude as those of the AFM-coupled interlayer skyrmion (Figure 5(b)).

When the driven current density j_d is too large ($> 5500 \times 10^{10} \text{ A/m}^2$), the Magnus force goes beyond the interlayer coupling strength, resulting in SkHE, i.e., decoupling of the merons in the upper and lower layers. The commonly used STT-driven current density range for skyrmions in experiments is $0.1\text{--}100 \times 10^{10} \text{ A/m}^2$,^{37,61,62} fall entirely within the range of $0.01\text{--}5500 \text{ A/m}^2$ for eliminating the SkHE. Figure 5(d) shows the straight motion of interlayer bimeron at a driven current density of $100 \times 10^{10} \text{ A/m}^2$, while Figure 5(e) shows the decoupling motion of the interlayer bimeron at a $j_d = 5500 \times 10^{10} \text{ A/m}^2$. Considering the presence of local defects, when an interlayer bimeron approaches the defect ($< 5 \text{ nm}$), its speed

decreases and can be pinned by the local defect, as shown in Figure S19. However, a large applied current can depin the interlayer bimeron, restoring the previous dynamic behavior.

In order to design promising materials and devices based on the interlayer bimeron in the future, several key steps must be taken. First, the system should meet symmetry conditions to generate interlayer bimeron, which can be achieved by stacking two homogeneous magnetic atomic layers or intercalating atoms in the middle of homogeneous magnetic bilayer, thereby ensuring the entire system possesses an inversion center i or mirror plane m_{xy}^\parallel ; then, large exchange interaction J and D can be achieved by materials selection to enhance the critical temperature of a stable interlayer bimeron. High Curie temperature 2D magnetic materials with in-plane ferromagnetism (large J) should be selected. Large D can be achieved by selecting 2D materials with heavy anions or heavy intercalated atoms.⁶³ Finally, a schematic diagram illustrating how to generate, manipulate, read, and delete information in a racetrack memory device based on the interlayer bimeron is shown in Figure S20.

In this work, we have proposed a new design principle to achieve a coupled topological magnetic structure with $Q = 0$, i.e., the SrDQ mechanism. Based on symmetry analysis, relationships are elaborately discussed between intra- and interlayer symmetry and D . In the MV_2Se_4 ($\text{M} = \text{Sr}, \text{Ba}$) systems, 5 types comprising ten $Q = 0$ topological magnetic structures were discovered. The topologically protected spin textures remain stable under finite external magnetic fields. For FM-coupled bilayer magnetic topological structures coupled with reversal D , we provided a general criterion for their

relationships with interlayer coupling and magnetocrystalline anisotropy K , also presented a phase diagram. In the current-driven spin dynamics, the elimination of SkHE of the interlayer bimeron is verified under a current density lower than $5500 \times 10^{10} \text{ A/m}^2$, and the FM-coupled interlayer bimeron exhibits a driven current density threshold of $0.01 \times 10^{10} \text{ A/m}^2$, an order of magnitude lower than the AFM-coupled interlayer biskyrmions. Beyond our studied MV_2Se_4 monolayer system, there remain many other unexplored SrDQ systems based on our symmetric design await further exploration, e.g., homojunction,⁶⁴ sandwich-like heterostructure,^{53,65} sandwich-like multiple atomic layered monolayer,⁶⁶ and so forth. Our design strategy can enrich the SkHE-free skyrmions family can enrich the design strategy and explain relationships between the spatial symmetry and topological magnetic structures over broad compositional spaces.

ASSOCIATED CONTENT

Supporting Information

The Supporting Information is available free of charge at <https://pubs.acs.org/doi/10.1021/acs.nanolett.4c02060>.

Derivation of DMI and symmetry; topological charge number Q and three characters of topological structures; relationship between Q and skyrmion Hall Effect (SkHE); derivation of the relationship among reversal D , interlayer coupling J_{bi} and Q ; eight structures of M intercalated into bilayer VSe_2 ; ground states of MV_2Se_4 ($M = \text{Sr}, \text{Ba}$); crystal field and the electric structure; band structures of MV_2Se_4 ; Curie temperature of MV_2Se_4 ; stabilities of MV_2Se_4 ; magnetocrystalline anisotropy of MV_2Se_4 ; coupling parameters of MV_2Se_4 ; DMI and SOC effect of MV_2Se_4 ; different U values; Monte Carlo simulations of interlayer bimeron under temperature field; micromagnetic simulations with local defects; computational methods ([PDF](#))

AUTHOR INFORMATION

Corresponding Authors

Shixuan Du — *Beijing National Laboratory for Condensed Matter Physics, Institute of Physics, Chinese Academy of Sciences, Beijing 100190, China; University of Chinese Academy of Sciences, Beijing 100049, China; Songshan Lake Materials Laboratory, Dongguan, Guangdong 523808, China; orcid.org/0000-0001-9323-1307; Email: sxdu@iphy.ac.cn*

Jinbo Pan — *Beijing National Laboratory for Condensed Matter Physics, Institute of Physics, Chinese Academy of Sciences, Beijing 100190, China; University of Chinese Academy of Sciences, Beijing 100049, China; Email: jpan@iphy.ac.cn*

Authors

Xudan Zhang — *Beijing National Laboratory for Condensed Matter Physics, Institute of Physics, Chinese Academy of Sciences, Beijing 100190, China; University of Chinese Academy of Sciences, Beijing 100049, China*

Guolin Wan — *Beijing National Laboratory for Condensed Matter Physics, Institute of Physics, Chinese Academy of Sciences, Beijing 100190, China; University of Chinese Academy of Sciences, Beijing 100049, China*

Jie Zhang — *University of Chinese Academy of Sciences, Beijing 100049, China*

Yan-Fang Zhang — *University of Chinese Academy of Sciences, Beijing 100049, China*

Complete contact information is available at:
<https://pubs.acs.org/10.1021/acs.nanolett.4c02060>

Notes

The authors declare no competing financial interest.

ACKNOWLEDGMENTS

We acknowledge the financial support from the National Natural Science Foundation of China (62488201, 52272172), the National Key Research and Development Program of China (2022YFA1204100), the Major Program of National Natural Science Foundation of China (92163206). Computational resources were provided by the National Supercomputing Center in Tianjin.

REFERENCES

- (1) Berg, B.; Luscher, M. Definition and statistic distribution of a topological number in the lattice $O(3)$ sigma-model. *Nucl. Phys. B* **1981**, *190* (2), 412–424.
- (2) Fert, A.; Reyren, N.; Cros, V. Magnetic skyrmions: advances in physics and potential applications. *Nat. Rev. Mater.* **2017**, *2* (7), 17031.
- (3) Zhang, X.; Zhou, Y.; Mee Song, K.; Park, T.-E.; Xia, J.; Ezawa, M.; Liu, X.; Zhao, W.; Zhao, G.; Woo, S. Skyrmion-electronics: writing, deleting, reading and processing magnetic skyrmions toward spintronic applications. *J. Phys.: Condens. Matter* **2020**, *32* (14), 143001.
- (4) Shao, Y. T.; Das, S.; Hong, Z. J.; Xu, R. J.; Chandrika, S.; Gómez-Ortiz, F.; García-Fernández, P.; Chen, L. Q.; Hwang, H. Y.; Junquera, J.; et al. Emergent chirality in a polar meron to skyrmion phase transition. *Nat. Commun.* **2023**, *14* (1), 1355.
- (5) Soda, M.; Forgan, E. M.; Blackburn, E.; Campillo, E.; Ryukhtin, V.; Hoffmann, I.; Kikkawa, A.; Taguchi, Y.; Yoshizawa, H.; Kawano-Furukawa, H. Asymmetric slow dynamics of the skyrmion lattice in MnSi. *Nat. Phys.* **2023**, *19*, 1476.
- (6) Yu, X. Z.; Onose, Y.; Kanazawa, N.; Park, J. H.; Han, J. H.; Matsui, Y.; Nagaosa, N.; Tokura, Y. Real-space observation of a two-dimensional skyrmion crystal. *Nature* **2010**, *465* (7300), 901–904.
- (7) Yu, X.; Kagawa, F.; Seki, S.; Kubota, M.; Masell, J.; Yasin, F. S.; Nakajima, K.; Nakamura, M.; Kawasaki, M.; Nagaosa, N.; et al. Real-space observations of 60-nm skyrmion dynamics in an insulating magnet under low heat flow. *Nat. Commun.* **2021**, *12* (1), 5079.
- (8) Fert, A.; Cros, V.; Sampaio, J. Skyrmions on the track. *Nat. Nanotechnol.* **2013**, *8* (3), 152–156.
- (9) Parkin, S.; Yang, S.-H. Memory on the racetrack. *Nat. Nanotechnol.* **2015**, *10* (3), 195–198.
- (10) He, B.; Tomasello, R.; Luo, X. M.; Zhang, R.; Nie, Z. Y.; Carpentieri, M.; Han, X. F.; Finocchio, G.; Yu, G. Q. All-electrical 9-bit skyrmion-based racetrack memory designed with laser irradiation. *Nano Lett.* **2023**, *23* (20), 9482–9490.
- (11) Singh, D.; Fujishiro, Y.; Hayami, S.; Moody, S. H.; Nomoto, T.; Baral, P. R.; Ukleev, V.; Cubitt, R.; Steinke, N. J.; Gawryluk, D. J.; et al. Transition between distinct hybrid skyrmion textures through their hexagonal-to-square crystal transformation in a polar magnet. *Nat. Commun.* **2023**, *14* (1), 8050.
- (12) Xia, J.; Zhang, X. C.; Liu, X. X.; Zhou, Y.; Ezawa, M. Universal quantum computation based on nanoscale skyrmion helicity qubits in frustrated magnets. *Phys. Rev. Lett.* **2023**, *130* (10), 106701.
- (13) Schöpf, J.; Thampi, A.; Milde, P.; Ivaneyko, D.; Kondovych, S.; Kononenko, D. Y.; Eng, L. M.; Jin, L.; Yang, L.; Wysocki, L.; et al. Neel skyrmion bubbles in $\text{La}_{0.7}\text{Sr}_{0.3}\text{Mn}_{1-x}\text{Ru}_x\text{O}_3$ multilayers. *Nano Lett.* **2023**, *23* (8), 3532–3539.
- (14) Yu, X. Z.; Koshibae, W.; Tokunaga, Y.; Shibata, K.; Taguchi, Y.; Nagaosa, N.; Tokura, Y. Transformation between meron and

- skyrmion topological spin textures in a chiral magnet. *Nature* **2018**, *564* (7734), 95–98.
- (15) Yu, X. Z.; Kanazawa, N.; Zhang, X. C.; Takahashi, Y.; Iakoubovskii, K. V.; Nakajima, K.; Tanigaki, T.; Mochizuki, M.; Tokura, Y. Spontaneous vortex-antivortex pairs and their topological transitions in a chiral-lattice magnet. *Adv. Mater.* **2024**, *36* (1), 2306441.
- (16) Amin, O. J.; Poole, S. F.; Reimers, S.; Barton, L. X.; Dal Din, A.; Maccherozzi, F.; Dhesi, S. S.; Novák, V.; Krizek, F.; Chauhan, J. S.; et al. Antiferromagnetic half-skyrmions electrically generated and controlled at room temperature. *Nat. Nanotechnol.* **2023**, *18* (8), 849–853.
- (17) Du, W. H.; He, Z. L.; Dou, K. Y.; Li, X. R.; Dai, Y.; Huang, B. B.; Ma, Y. D. Chiral magnetic quasiparticles with zero topological charge in 2D lattice. *Adv. Funct. Mater.* **2024**, 2400971.
- (18) Li, X. G.; Shen, L. C.; Bai, Y. H.; Wang, J. L.; Zhang, X. C.; Xia, J.; Ezawa, M.; Tretiakov, O. A.; Xu, X. H.; Mruczkiewicz, M.; et al. Bimeron clusters in chiral antiferromagnets. *npj Comput. Mater.* **2020**, *6* (1), 169.
- (19) Rosales, H. D.; Albarracín, F. A. G.; Pujol, P.; Jaubert, L. D. C. Skyrmion fluid and bimeron glass protected by a chiral spin liquid on a kagome lattice. *Phys. Rev. Lett.* **2023**, *130* (10), 106703.
- (20) Sun, W.; Wang, W.; Li, H.; Zhang, G.; Chen, D.; Wang, J.; Cheng, Z. Controlling bimerons as skyrmion analogues by ferroelectric polarization in 2D van der Waals multiferroic heterostructures. *Nat. Commun.* **2020**, *11* (1), 5930.
- (21) Cui, Q.; Zhu, Y.; Jiang, J.; Liang, J.; Yu, D.; Cui, P.; Yang, H. Ferroelectrically controlled topological magnetic phase in a Janus-magnet-based multiferroic heterostructure. *Phys. Rev. Res.* **2021**, *3* (4), No. 043011.
- (22) Tang, J.; Wu, Y. D.; Jiang, J. L.; Kong, L. Y.; Liu, W.; Wang, S. G.; Tian, M. L.; Du, H. F. Sewing skyrmion and antiskyrmion by quadrupole of Bloch points. *Sci. Bull.* **2023**, *68* (23), 2919–2923.
- (23) Li, S.; Ezawa, M.; Zhou, Y. Current-induced dynamics of isolated antiferromagnetic antiskyrmion and antiskyrmionium. *Phys. Rev. B* **2023**, *107* (17), 174409.
- (24) Göbel, B.; Schäffer, A. F.; Berakdar, J.; Mertig, I.; Parkin, S. S. P. Electrical writing, deleting, reading, and moving of magnetic skyrmioniums in a racetrack device. *Sci. Rep.* **2019**, *9* (1), 12119.
- (25) Yu, X. Z.; Tokunaga, Y.; Kaneko, Y.; Zhang, W. Z.; Kimoto, K.; Matsui, Y.; Taguchi, Y.; Tokura, Y. Biskyrmion states and their current-driven motion in a layered Manganite. *Nat. Commun.* **2014**, *5*, 3198.
- (26) Reichhardt, C.; Reichhardt, C. J. O.; Milosevic, M. V. Statics and dynamics of skyrmions interacting with disorder and nanostructures. *Rev. Mod. Phys.* **2022**, *94* (3), No. 035005.
- (27) Zhang, X.; Zhou, Y.; Ezawa, M. Magnetic bilayer-skyrmions without skyrmion Hall effect. *Nat. Commun.* **2016**, *7* (1), 10293.
- (28) Barker, J.; Tretiakov, O. A. Static and dynamical properties of antiferromagnetic skyrmions in the presence of applied current and temperature. *Phys. Rev. Lett.* **2016**, *116* (14), 147203.
- (29) Nagaosa, N.; Tokura, Y. Topological properties and dynamics of magnetic skyrmions. *Nat. Nanotechnol.* **2013**, *8* (12), 899–911.
- (30) Jiang, W. J.; Zhang, X. C.; Yu, G. Q.; Zhang, W.; Wang, X.; Jungfleisch, M. B.; Pearson, J. E.; Cheng, X. M.; Heinonen, O.; Wang, K. L.; et al. Direct observation of the skyrmion Hall effect. *Nat. Phys.* **2017**, *13* (2), 162–169.
- (31) Zeissler, K.; Finizio, S.; Barton, C.; Huxtable, A. J.; Massey, J.; Raabe, J.; Sadovnikov, A. V.; Nikitov, S. A.; Brearton, R.; Hesjedal, T.; et al. Diameter-independent skyrmion Hall angle observed in chiral magnetic multilayers. *Nat. Commun.* **2020**, *11* (1), 428.
- (32) Göbel, B.; Mertig, I.; Tretiakov, O. A. Beyond skyrmions: review and perspectives of alternative magnetic quasiparticles. *Phys. Rep.* **2021**, *895*, 1–28.
- (33) Braun, H. B. Topological effects in nanomagnetism: from superparamagnetism to chiral quantum solitons. *Adv. Phys.* **2012**, *61* (1), 1–116.
- (34) Hirata, Y.; Kim, D. H.; Kim, S. K.; Lee, D. K.; Oh, S. H.; Kim, D. Y.; Nishimura, T.; Okuno, T.; Futakawa, Y.; Yoshikawa, H.; et al. Vanishing skyrmion Hall effect at the angular momentum compensation temperature of a ferrimagnet. *Nat. Nanotechnol.* **2019**, *14* (3), 232–236.
- (35) Legrand, W.; Maccariello, D.; Ajejas, F.; Collin, S.; Vecchiola, A.; Bouzehouane, K.; Reyren, N.; Cros, V.; Fert, A. Room-temperature stabilization of antiferromagnetic skyrmions in synthetic antiferromagnets. *Nat. Mater.* **2020**, *19* (1), 34–42.
- (36) Dai, B.; Wu, D.; Razavi, S. A.; Xu, S.; He, H.; Shu, Q.; Jackson, M.; Mahfouzi, F.; Huang, H.; Pan, Q.; et al. Electric field manipulation of spin chirality and skyrmion dynamic. *Sci. Adv.* **2023**, *9* (7), No. eade6836.
- (37) He, Z.; Li, Z.; Chen, Z.; Wang, Z.; Shen, J.; Wang, S.; Song, C.; Zhao, T.; Cai, J.; Lin, S.-Z.; et al. Experimental observation of current-driven antiskyrmion sliding in stripe domains. *Nat. Mater.* **2024**, *23*, 1048–1054.
- (38) Dzyaloshinsky, I. A thermodynamic theory of weak ferromagnetism of antiferromagnetics. *J. Phys. Chem. Solids* **1958**, *4* (4), 241–255.
- (39) Moriya, T. Anisotropic superexchange interaction and weak ferromagnetism. *Phys. Rev.* **1960**, *120* (1), 91–98.
- (40) Yang, H. X.; Liang, J. H.; Cui, Q. R. First-principles calculations for Dzyaloshinskii-Moriya interaction. *Nat. Rev. Phys.* **2023**, *5* (1), 43–61.
- (41) Liang, J.; Cui, Q.; Yang, H. Electrically switchable Rashba-type Dzyaloshinskii-Moriya interaction and skyrmion in two-dimensional magnetoelectric multiferroics. *Phys. Rev. B* **2020**, *102* (22), 220409.
- (42) Shao, Z.; Liang, J.; Cui, Q.; Chshiev, M.; Fert, A.; Zhou, T.; Yang, H. Multiferroic materials based on transition-metal dichalcogenides: potential platform for reversible control of Dzyaloshinskii-Moriya interaction and skyrmion via electric field. *Phys. Rev. B* **2022**, *105* (17), 174404.
- (43) Yu, D. X.; Ga, Y. L.; Liang, J. H.; Jia, C. L.; Yang, H. X. Voltage-controlled Dzyaloshinskii-Moriya interaction torque switching of perpendicular magnetization. *Phys. Rev. Lett.* **2023**, *130* (5), No. 056701.
- (44) Ryu, K.-S.; Thomas, L.; Yang, S.-H.; Parkin, S. Chiral spin torque at magnetic domain walls. *Nat. Nanotechnol.* **2013**, *8* (7), 527–533.
- (45) Kim, S. K. Dynamics of bimeron skyrmions in easy-plane magnets induced by a spin supercurrent. *Phys. Rev. B* **2019**, *99* (22), 224406.
- (46) Emori, S.; Bauer, U.; Ahn, S. M.; Martinez, E.; Beach, G. S. D. Current-driven dynamics of chiral ferromagnetic domain walls. *Nat. Mater.* **2013**, *12* (7), 611–616.
- (47) Wang, L.; Shi, Y.; Liu, M.; Zhang, A.; Hong, Y.-L.; Li, R.; Gao, Q.; Chen, M.; Ren, W.; Cheng, H.-M.; et al. Intercalated architecture of MA_2Z_4 family layered van der Waals materials with emerging topological, magnetic and superconducting properties. *Nat. Commun.* **2021**, *12* (1), 2361.
- (48) Xiao, B. W.; Zheng, Y.; Song, M.; Liu, X.; Lee, G. H.; Omenya, F.; Yang, X.; Engelhard, M. H.; Reed, D.; Yang, W. L.; et al. Protonation stimulates the layered to rock salt phase transition of Ni-rich sodium cathodes. *Adv. Mater.* **2024**, *36*, 2308380.
- (49) Yin, Y. G.; Lian, C. S.; Meng, F. Q.; Liu, Y. W.; Chen, W.; Ji, L. C.; Zhou, X. Y.; Zhang, Z. C.; Zhang, Q. H.; Gu, L.; et al. Quenched charge density wave and large in-plane upper critical field of self-intercalated bilayer $NbSe_2$. *Phys. Rev. B* **2023**, *108* (4), No. L041405.
- (50) Wong, P. K. J.; Zhang, W.; Bussolotti, F.; Yin, X. M.; Herng, T. S.; Zhang, L.; Huang, Y. L.; Vinai, G.; Krishnamurthy, S.; Bukhvalov, D. W.; et al. Evidence of spin frustration in a Vanadium diselenide monolayer magnet. *Adv. Mater.* **2019**, *31* (23), 1901185.
- (51) Bonilla, M.; Kolekar, S.; Ma, Y. J.; Diaz, H. C.; Kalappattil, V.; Das, R.; Eggers, T.; Gutierrez, H. R.; Phan, M. H.; Batzill, M. Strong room-temperature ferromagnetism in VSe_2 monolayers on van der Waals substrates. *Nat. Nanotechnol.* **2018**, *13* (4), 289–293.
- (52) Zhang, Z. P.; Niu, J. J.; Yang, P. F.; Gong, Y.; Ji, Q. Q.; Shi, J. P.; Fang, Q. Y.; Jiang, S. L.; Li, H.; Zhou, X. B.; et al. van der Waals epitaxial growth of 2D metallic Vanadium diselenide single crystals

and their extra-high electrical conductivity. *Adv. Mater.* **2017**, *29* (37), 1702359.

(53) Khan, I.; Marfoua, B.; Hong, J. Optical transparency in 2D ferromagnetic WSe₂/1T-VSe₂/WSe₂ multilayer with strain induced large anomalous Nernst conductivity. *Nanotechnology* **2024**, *35* (12), 125704.

(54) Pathirage, V.; Khatun, S.; Lisenkov, S.; Lasek, K.; Li, J.; Kolekar, S.; Valvidares, M.; Gargiani, P.; Xin, Y.; Ponomareva, I.; et al. 2D materials by design: intercalation of Cr or Mn between two VSe₂ van der Waals layers. *Nano Lett.* **2023**, *23* (20), 9579–9586.

(55) Sabani, D.; Bacaksiz, C.; Milosevic, M. V. *Ab initio* methodology for magnetic exchange parameters: generic four-state energy mapping onto a Heisenberg spin Hamiltonian. *Phys. Rev. B* **2020**, *102* (1), No. 014457.

(56) Xiang, H. J.; Lee, C.; Koo, H. J.; Gong, X. G.; Whangbo, M. H. Magnetic properties and energy-mapping analysis. *Dalton Trans.* **2013**, *42* (4), 823–853.

(57) Xu, C.; Xu, B.; Dupé, B.; Bellaiche, L. Magnetic interactions in BiFeO₃: a first-principles study. *Phys. Rev. B* **2019**, *99* (10), 104420.

(58) Xu, C.; Chen, P.; Tan, H.; Yang, Y.; Xiang, H.; Bellaiche, L. Electric-field switching of magnetic topological charge in type-I multiferroics. *Phys. Rev. Lett.* **2020**, *125* (3), No. 037203.

(59) Du, W. H.; Dou, K. Y.; He, Z. L.; Dai, Y.; Huang, B. B.; Ma, Y. D. Spontaneous magnetic skyrmions in single-layer CrInX₃ (X = Te, Se). *Nano Lett.* **2022**, *22* (8), 3440–3446.

(60) Kabiraj, A.; Mahapatra, S. Realizing unipolar and bipolar intrinsic skyrmions in MXenes from high-fidelity first-principles calculations. *npj Comput. Mater.* **2023**, *9* (1), 173.

(61) Yamanouchi, M.; Chiba, D.; Matsukura, F.; Ohno, H. Current-induced domain-wall switching in a ferromagnetic semiconductor structure. *Nature* **2004**, *428* (6982), 539–542.

(62) Thomas, L.; Moriya, R.; Rettner, C.; Parkin, S. S. P. Dynamics of Magnetic Domain Walls Under Their Own Inertia. *Science* **2010**, *330* (6012), 1810–1813.

(63) Wei, W.-S.; He, Z.-D.; Qu, Z.; Du, H.-F. Dzyaloshinsky–Moriya interaction (DMI)-induced magnetic skyrmion materials. *Rare Met.* **2021**, *40* (11), 3076–3090.

(64) Li, Q.; Wang, Z.; Ma, J.; Han, M.; Gao, P.; Cai, M.; Zhang, Y.; Song, Y.; Peng, S. Unveiling the surface-interface properties of perovskite crystals and pivotal regulation strategies. *Nano Res.* **2024**, *17*, 3950.

(65) Hou, Y. S.; Xue, F.; Qiu, L.; Wang, Z.; Wu, R. Q. Multifunctional two-dimensional van der Waals Janus magnet Cr-based dichalcogenide halides. *npj Comput. Mater.* **2022**, *8* (1), 120.

(66) Wang, L.; Shi, Y. P.; Liu, M. F.; Zhang, A.; Hong, Y. L.; Li, R. H.; Gao, Q.; Chen, M. X.; Ren, W. C.; Cheng, H. M.; et al. Intercalated architecture of MA₂Z₄ family layered van der Waals materials with emerging topological, magnetic and superconducting properties. *Nat. Commun.* **2021**, *12* (1), 2361.